



RESEARCH ARTICLE

ECMWF SSW forecast evaluation using infrasound

10.1002/2015JD024251

Both authors P. S. M. Smets and J. D. Assink contributed equally.

Key Points:

- A novel method for forecast evaluation in the middle atmosphere is proposed
- Infrasound provides independent measurements to improve the middle/upper atmospheric coverage
- SSW onset is better predicted by the 10 day forecast, duration by the nowcast

Supporting Information:

- Supporting Information S1
- Figure S1

Correspondence to:

P. S. M. Smets,
pieter.smets@knmi.nl

Citation:

Smets P. S. M., J. D. Assink, A. Le Pichon, and L. G. Evers (2016), ECMWF SSW forecast evaluation using infrasound, *J. Geophys. Res. Atmos.*, 121, doi:10.1002/2015JD024251.

Received 22 SEP 2015

Accepted 13 APR 2016

Accepted article online 21 APR 2016

©2016. The Authors.

This is an open access article under the terms of the Creative Commons Attribution-NonCommercial-NoDerivs License, which permits use and distribution in any medium, provided the original work is properly cited, the use is non-commercial and no modifications or adaptations are made.

P. S. M. Smets^{1,2}, J. D. Assink^{1,3}, A. Le Pichon³, and L. G. Evers^{1,2}

¹R&D Department of Seismology and Acoustics, Royal Netherlands Meteorological Institute (KNMI), De Bilt, Netherlands, ²Department of Geoscience and Engineering, Faculty of Civil Engineering and Geosciences, Delft University of Technology, Delft, Netherlands, ³CEA, DAM, DIF, Arpajon, France

Abstract Accurate prediction of Sudden Stratospheric Warming (SSW) events is important for the performance of numerical weather prediction due to significant stratosphere-troposphere coupling. In this study, for the first time middle atmospheric numerical weather forecasts are evaluated using infrasound. A year of near-continuous infrasound from the volcano Mount Tolbachik (Kamchatka, Russian Federation) is compared with simulations using high-resolution deterministic forecasts of the European Centre for Medium-Range Weather Forecasts (ECMWF). For the entire time span the nowcast generally performs best, indicated by a higher continuity of the predicted wavefront characteristics with a minimal back azimuth difference. Best performance for all forecasts is obtained in summer. The difference between the infrasound observations and the predictions based on the forecasts is significantly larger during the 2013 SSW period for all forecasts. Simulations show that the SSW onset is better captured by the 10 day forecast while the recovery is better captured by the nowcast.

1. Introduction

The middle atmosphere has gained more and more importance for the purpose of weather and climate prediction, since increasing evidence indicates that the troposphere and stratosphere are more closely coupled than assumed before [Baldwin and Dunkerton, 2001; Charlton et al., 2004; Shaw and Shepherd, 2008]. Significant effort has been made toward a more comprehensive representation of the atmosphere to better capture the stratospheric variability as well as the stratospheric-tropospheric interactions [Randel et al., 2004; Charlton-Perez et al., 2013].

The strongest manifestations of this stratosphere-troposphere coupling are Sudden Stratospheric Warmings (SSWs) [Charlton and Polvani, 2007; Gerber et al., 2009]. SSWs are regularly occurring features of the winter stratosphere on the Northern Hemisphere, characterized by dramatic changes in the stratospheric wind and temperature. The importance of accurately predicting SSWs is justified by the delayed impact up to 2 months that such events have on the weather as experienced on the Earth's surface [Sigmond et al., 2013]. However, significant discrepancies between numerical weather prediction models and the observations they assimilate may lead to rejection of good data by the data assimilation system which means that both the forecasts and analyses of SSWs will likely be inadequate. Recently, the European Centre for Medium-Range Weather Forecasts (ECMWF) has adapted its numerical scheme that reduces this problem, leading to an improved characterization of SSWs [Diamantakis, 2014]. Besides such numerical adaptations, further improvements in SSW predictions can be obtained from better resolving the stratosphere [Gerber et al., 2009; Roff et al., 2011] and mesosphere [Coy et al., 2011] as well as assimilating data from these regions, which have been notoriously difficult to monitor [Ramaswamy et al., 2001]. Only temperature can be resolved by satellites, dominated by Advanced Microwave Sounding Unit type A (AMSU-A) observations, available by more than a dozen satellites, and are directly assimilated in the ECMWF models. In a recent study [Le Pichon et al., 2015], colocated independent ground-based middle atmospheric wind and temperature measurements have been compared to both the ECMWF operational analyses and NASA's Modern Era Retrospective analysis for Research and Applications (MERRA) reanalyses. Significant discrepancies were identified in the region above 40 km in winter as well as for variability on shorter timescales (2–15 day period) above 30 km. Thus, SSWs are a good starting point to apply novel techniques based on infrasonic analysis.

Since the pioneering work of *Donn and Rind* [1972], there has been much development in the use of ground-based infrasound arrays for upper atmospheric remote sensing [*Le Pichon et al.*, 2005; *Lalande et al.*, 2012; *Assink et al.*, 2013; *Fricke et al.*, 2014; *Chunchuzov et al.*, 2015]. An important application of this technique is the evaluation of atmospheric analyses [*Assink et al.*, 2014a] and ensemble members [*Smets et al.*, 2015]. Recently, various passive acoustic remote sensing studies have focused on SSW events [*Evers and Siegmund*, 2009; *Evers et al.*, 2012; *Assink et al.*, 2014b; *Smets and Evers*, 2014].

Volcanoes represent valuable sources for passive acoustic remote sensing of the atmosphere, as the source location is fixed and the source is relatively well understood [*Fee et al.*, 2010; *Matoza et al.*, 2011; *Marchetti et al.*, 2013]. Here a novel method for the evaluation of middle atmospheric weather forecasts is introduced, using near-continuous infrasound detections from Mount Tolbachik on the Kamchatka peninsula in Russian Federation (55.8°N, 160.3°E). The relative small wavelength and near-continuous character of the source leads to high spatiotemporal resolution evaluations and improved insight in the forecast capabilities in the middle atmosphere, in particular, during SSW events. In addition, it is demonstrated that infrasound can provide useful additional information on SSW onset and duration.

The article is organized as follows. Section 2 sets out the fundamentals of infrasound as an atmospheric remote sensing technique, including the signature of SSW events on infrasound recordings. Section 3 explains the methods in more detail, covering infrasound observations, propagation modeling, and the atmospheric specifications. Section 4 describes the observations, followed by the evaluation of ECMWF forecasts in section 5 with distinction between the entire observation period and the 2013 SSW. Discussion and conclusions are stated in section 6.

2. Background

2.1. The Relationship Between Wind, Temperature, and Infrasound

Infrasound, or low-frequency acoustic waves, is generated by movement of large volumes of air. Such movements can be created by natural or anthropogenic sources. Examples include interfering ocean waves, volcanic eruptions, (nuclear) explosions, and meteor explosions [*Brachet et al.*, 2010]. Infrasound can propagate efficiently over long ranges, since attenuation is relatively low. Moreover, several wave guides exist between the Earth's surface and the (upper) atmosphere that channel infrasonic energy.

One can distinguish between tropospheric, stratospheric, and thermospheric waveguides. The tropospheric waveguide is bound by the jet stream around the tropopause (~10 km). The stratospheric waveguide is formed by the temperature increase due to the presence of ozone and the circumpolar vortex. Generally, the stratospheric waveguide extends to ~50 km during the boreal summer. During SSWs, the top of the waveguide may descend into the lower stratosphere and may even extend into the lower mesosphere. The thermospheric waveguide exists due to the strong temperature gradient above the mesopause. However, infrasound is much attenuated at thermospheric altitudes [*Assink et al.*, 2012].

Sound propagation in the atmosphere is a function of wind \mathbf{w} and temperature T , which may vary strongly as a function of location and time. For a fixed source-receiver pair, changes in the mode of propagation (i.e., stratospheric to thermospheric) can be observed as horizontal wind and temperature change seasonally. Ray tracing (Figure 1) can be used to model the influence of 3-D temperature and three-component wind fields on infrasound propagation [*Brekhovskikh and Godin*, 1999].

It is instructive to consider a horizontally layered atmosphere to review basic concepts of infrasound propagation. The effective sound speed c_{eff} can be used to approximate to first order [*Godin*, 2002] the effects of temperature T and horizontal wind \mathbf{w}_{uv} in the direction of propagation ϕ :

$$\begin{aligned} c_{\text{eff}}(z) &= \sqrt{\gamma RT(z)} + |\mathbf{w}_{uv}(z)| \cos(\phi - \phi_{\mathbf{w}_{uv}}(z)) \\ &= c_T(z) + w_a(z) \end{aligned} \quad (1)$$

Here $\gamma = 1.4$ and $R = 286.9 \text{ J kg}^{-1} \text{ K}^{-1}$ are the ratio of specific heats and the specific gas constant for dry air, respectively. Note that both propagation azimuth ϕ and wind direction $\phi_{\mathbf{w}_{uv}}$ are clockwise relative to the north. From Snell's law, it follows that positive vertical gradients of the effective sound speed lead to downward refraction, and vice versa. Acoustic waveguides are combinations of these gradients. The orientation of the source and receiver locations determine the propagation azimuth ϕ . This angle is used to estimate

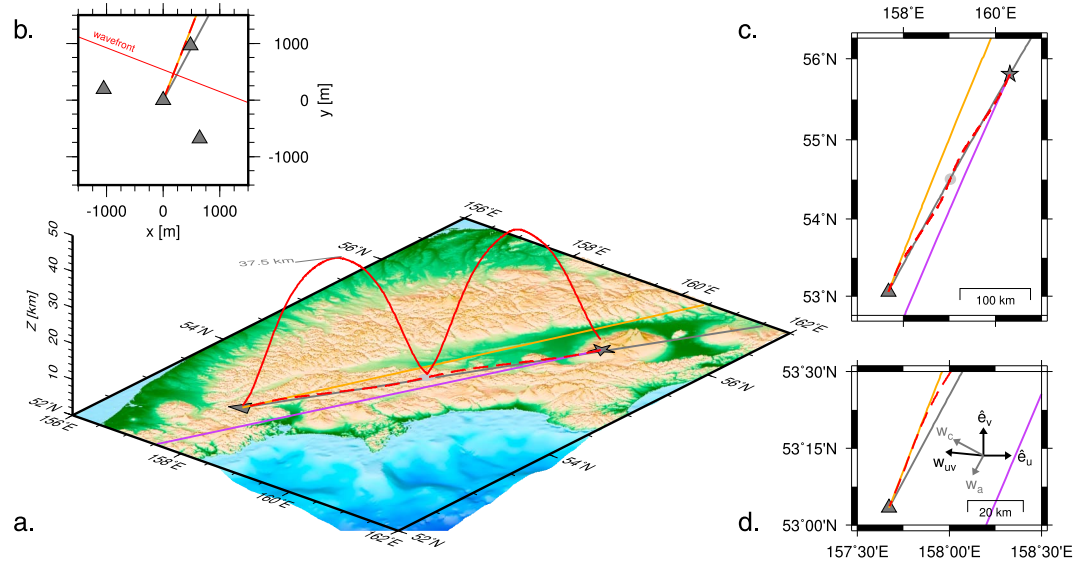


Figure 1. (a) Three-dimensional map of the Kamchatka peninsula in Russian Federation (55.8°N, 160.3°E), showing source (star) and receiver array (triangle) locations interconnected with an example eigenray (solid red line) and its horizontal projection (dashed red line). The purple, orange, and gray lines represent the azimuth, back azimuth, and theoretical back azimuth angles, respectively. (b) IS44 array elements layout (triangles) with theoretical, observed, and ray simulated back azimuth angles, all with respect to the array central element. The thin red line perpendicular to the observed back azimuth indicates the incoming planar wavefront. (c) Horizontal projection (top view) of Figure 1a with the gray circle indicating the reflection at the ground. (d) Zoom-in in Figure 1c, showing the receiver area with the observed and theoretical back azimuth angles. The black vectors indicate the zonal and meridional wind unit vectors \hat{e}_u and \hat{e}_v and the horizontal wind vector \mathbf{w}_{uv} at 37.5 km altitude. Its projection along the theoretical back azimuth, approximating the propagation direction, is given by the gray vectors resulting in the along-track w_a and cross-wind w_c components. The purple and orange lines change due to variations in the atmosphere while the solid gray line is constant.

the along-track wind (w_a) and cross-wind (w_c) components, by rotating the zonal (w_u) and meridional (w_v) components of the horizontal wind vector \mathbf{w}_{uv} (see Figure 1d)

$$\begin{pmatrix} w_a \\ w_c \end{pmatrix} = \begin{pmatrix} \sin \phi & \cos \phi \\ -\cos \phi & \sin \phi \end{pmatrix} \begin{pmatrix} w_u \\ w_v \end{pmatrix} \quad (2)$$

The quantities w_a and w_c each have a specific influence on infrasound propagation.

Infrasound is often measured with arrays of microbarometers (Figure 1b). Beamforming techniques allow for the detection of coherent infrasound and the estimation of the *slowness vector* $\mathbf{s} = \{s_x, s_y, s_z\}$. The slowness vector describes the direction of propagation of a wavefront in three dimensions. The magnitude of slowness corresponds to the reciprocal of wave propagation speed. The slowness vector can be converted into azimuth ϕ and trace velocity c_{trc} as

$$\phi = \arctan \frac{s_x}{s_y} \quad (3)$$

$$c_{trc} = \frac{1}{|\mathbf{s}_{xy}|} = \frac{1}{|\mathbf{s}| \cos \theta} = \frac{c_{rcv}}{\cos \theta} \quad (4)$$

In observational studies, *back azimuth* is used instead of azimuth (equation (3)), taking the array as the point of reference. It is often found that significant deviations exist between the observed and theoretical back azimuth. Such deviations exist due to the influence of cross winds w_c and are like the crabbing of an airplane needed to fly along a constant bearing in a cross wind. Back azimuth deviation is illustrated in Figure 1c, as the angle between the true azimuth (gray line) and the propagation azimuth (purple line) needed to arrive at the receiver location. Note that the propagation path is denoted by the dashed red line. At the receiver location, the observed back azimuth (orange line) does not point toward the source. Only in the case of zero cross wind, all four mentioned lines would align.

Trace velocity (equation (4)) is the horizontal projection of the propagation velocity vector and describes the horizontal propagation speed of a wavefront with grazing angle θ . This quantity is of interest observationally, as infrasound arrays are typically constructed horizontally. For a layered medium, trace velocity is an invariant [Pierce, 1981].

Finally, return height z_r is defined as an altitude at which sound refracts down from the upper atmosphere toward the Earth's surface. From the definition of trace velocity and its invariance, it follows that the trace velocity equals the effective sound speed at the return height. This relationship allows one to identify return heights from an effective sound speed profile. A range of return heights may exist, but z_r is necessarily smaller or equal to the top of the acoustic waveguide. For the ray shown in Figure 1a, z_r is estimated to be around 37.5 km.

In summary, ignoring vertical wind, in-plane atmospheric specifications (temperature, along-track wind) determine effective sound speed and therefore trace velocity, while the cross-track winds determine the back azimuth deviation. Thus, a complementary set of infrasound observations exist that is sensitive to temperature and horizontal wind.

2.2. Signature of SSW Events on Infrasound Recordings

Infrasound has a long history as a method to monitor changes in the stratospheric polar vortex wind direction dedicated to SSWs. Already in the early 1970s, various pioneering studies of Donn and Rind describe the infrasonic signature of a SSW [Donn and Rind, 1971, 1972, Rind and Donn, 1975; Rind, 1978]. Using ambient coherent noise, microbaroms, as a continuously natural mechanism for probing the upper atmosphere, they relate abnormal winter amplitude intensities to SSW events. However, these studies came to a stop when nuclear tests were diverted to the subsurface under the Limited or Partial Test Ban Treaty. Recently, with the signature of the Comprehensive Nuclear-Test-Ban Treaty, the use of infrasound as a passive atmospheric probe gained renewed attention. More recently, Evers and Siegmund [2009] used coherent ambient noise to identify signals arriving from the opposite direction than expected under regular winter conditions to characterize the infrasonic signature of the 2009 major SSW, whereas Assink *et al.* [2014b] identified simultaneous arrivals from two stratospheric ducts due to the 2011 minor SSW. The temperature effect of a hot stratosphere during a SSW on infrasound propagation is studied by Evers *et al.* [2012]. During the 2010 SSW, the extent of the classical stratospheric shadow zone (~ 200 km) reduces by a factor of 2, leading to extremely small shadow zones. Smets and Evers [2014] demonstrated the use of ambient noise amplitude variations to describe the life cycle of the 2009 major SSW. Similar to the earlier study of Donn and Rind [1972], amplitude variations allow to estimate the return height. In addition, Smets and Evers [2014] demonstrated that the combined signature of the change in back azimuth direction, solar tidal signature type, and/or phase variation of the amplitude variation of the observed microbaroms reveals the type of vortex disturbance, either split or reversal.

3. Methods

In this work, simulated and observed infrasound wavefront parameters are compared, i.e., back azimuth and trace velocity. The theoretical basis of this method relies on the assertion that sound propagates through a particular atmospheric state. The atmospheric state that is closest to reality will then lead to simulated values that are closest to the observed values.

Experimental evidence for the validity of this method has been provided by various earlier studies [e.g., Le Pichon *et al.*, 2005; Assink *et al.*, 2014a; Smets *et al.*, 2015].

For this study, infrasound propagation is simulated from the volcano Mount Tolbachik to a regional infrasound station at 347 km distance (Figure 1), for comparison with observations. The remainder of this section describes the observations, the propagation method, and the atmospheric specifications that are used.

3.1. Infrasound Observations

Observations from infrasound station IS44 (Kamchatka, Russian Federation) are used. IS44 is part of the International Monitoring System (IMS). The IMS is a global network of infrasound, seismic, hydroacoustic, and radionuclide stations for the verification of the Comprehensive Nuclear-Test-Ban Treaty (CTBT) [Dahlman *et al.*, 2009]. Today, 45 out of 60 infrasound stations have been installed and certified, providing continuous recordings of infrasound worldwide.

Table 1. Parameters Used to Filter the Relevant Detections of Mount Tolbachik From the Raw IDC Bulletins [Brachet et al., 2010]

| Parameter | Range |
|--------------------------|-----------------------------------|
| Mean frequency | 0.5–3.5 Hz |
| Back azimuth ψ | $28.11 \pm 12^\circ$ |
| σ_ψ | $<2.0^\circ$ |
| Trace velocity c_{trc} | $310\text{--}450\text{ m s}^{-1}$ |
| $\sigma_{c_{trc}}$ | $<25.0\text{ m s}^{-1}$ |
| Consistency | $<0.15\text{ s}$ |

IS44 consists of four MB2000 microbarometers [Ponceau and Bosca, 2010] that measure small pressure fluctuations on the order of mPa up to tens of pascals. The microbarometers have a flat response over the frequency band spanning from 0.08 to 4 Hz and are sampled at 20 Hz. Wind noise filters are used to reduce noise levels over the infrasonic frequency band, by spatially averaging the pressure field in the vicinity of an infrasound sensor.

Infrasound detection bulletins are provided by the International Data Centre (IDC) of the CTBT Organization (CTBTO). The bulletins include infrasound waveform parameters (including their uncertainties) as a function of time, such as back azimuth, trace velocity, and dominant frequency. The bulletins correspond to average values of grouped detections in time-frequency space [Brachet et al., 2010]. The parameters used to filter the relevant detections from the raw IDC bulletins are given in Table 1.

3.2. Propagation Modeling

For the evaluation, an in-house developed ray tracing algorithm (cast in spherical coordinates) is used that takes into account the full effect of the 3-D inhomogeneous wind and temperature fields, see, for example, Brekhovskikh and Godin [1999]. See Figure 2 as an example of stratospheric infrasound propagation using 3-D ray theory. For every atmospheric model, eigenrays (connecting source and receiver, see Figure 1 a) are

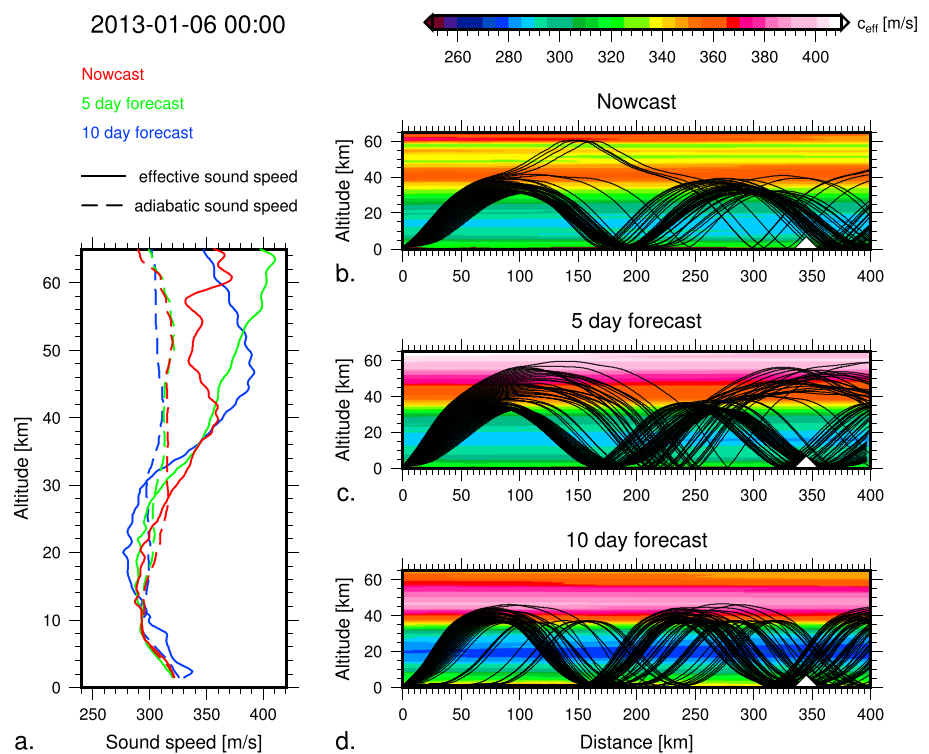


Figure 2. (a) Sound speed profiles derived from ECMWF HRES forecasts for 6 January 2013 at 00 UTC indicating the (dashed) adiabatic and (solid) effective sound speed at the source. While the largest variability between the forecasts is found in the upper stratosphere, the 10 day forecast is different throughout the troposphere and lower stratosphere as well. The three panels on the right show 3-D ray trace infrasound propagation over 400 km using three different ECMWF HRES forecasts: (b) nowcast, (c) 5 day forecast, and (d) 10 day forecast. The background corresponds to the effective sound speed, and the white triangle indicates the array distance. The temperature and wind variability in the profiles are reflected in the far-field infrasound predictions.

considered for further analysis. Given the aperture of IS44, rays that pass within 1 km of the center of the array are counted as eigenrays. For every eigenray, trace velocity and back azimuth deviation values are stored, for comparison with the observed values.

Except for the limitations that are inherent to the ray theory approximation [Brekhovskikh and Godin, 1999], namely, that the variations in atmospheric wind and temperature are small over an acoustic wavelength, the theory is exact. Thus, the propagation effects such as diffraction and scattering from small-scale structure (e.g., from gravity waves) [Chunchuzov *et al.*, 2015] are neglected. These effects are included in full-wave modeling [e.g., Assink *et al.*, 2014a]. Typically, such computations are limited to in-plane effects, because of the additional high computational load for out-of-plane effects.

3.3. Atmospheric Specifications

In this study, ECMWF's operational high spatial resolution forecasts (HRES), part of the Integrated Forecast System (IFS) cycle 38r1 (June 2012) and cycle 38r2 (June 2013) are used. The IFS consists of a general circulation model and assimilates radiosonde-, ground-, and satellite-based atmospheric observations by four-dimensional variational assimilation (4D-Var). HRES is the deterministic and highest spatial resolution member of the IFS with a resolution of $T_L1279L91$; horizontal resolution of ~ 16 km or 0.125° and 91 vertical levels up to 0.01 hPa, increased to 137 levels in June 2013. See *European Centre for Medium-Range Weather Forecasts* [2016] for the evolution of the IFS. Forecasts are available every 12 h with a forecast step up to 10 days. For this study, 3-D atmospheric specifications of wind, temperature, humidity, and pressure are used every 12 h for the 0 (nowcast), 5 and 10 day forecasts. All specifications are vertically resampled to 500 m levels from ground up to 70 km. Consequentially, infrasound propagation above 70 km cannot be simulated using the ECMWF IFS. To obtain mesospheric and thermospheric returns, the ECMWF forecasts are extended above 70 km by splining a 1-D wind and temperature profile obtained from the Horizontal Wind Model (HWM) and Mass Spectrometer and Incoherent Radar Model (MSIS) semi-empirical models [Drob and *et al.*, 2008; Picone *et al.*, 2002], for the midpoint between source and receiver.

4. Observations

Figure 3 shows four states of the analysis temperature and wind field in the Northern Hemisphere at 5.0 hPa (about 36 km altitude), prior to the 2013 major SSW (first column), during the SSW (second and third columns), and during the summer of 2013 (fourth column).

Prior to the SSW, the circumpolar vortex flows eastward around the Arctic region, thereby sustaining a cold Arctic stratosphere. This typical winter situation is disturbed during the first week of January 2013. As a result of upward propagating planetary waves, e.g., Matsuno [1971] and Baldwin and Dunkerton [2001], the circumpolar vortex weakens and destabilizes, migrates south of 65°N , and finally is split into two daughter vortices. As a result, the vortex direction is reversed for various regions. Additionally, the Arctic stratosphere warms up to 50°C within a few days, classifying the warming as major. After 18 January 2013, the stratosphere on the Northern Hemisphere returns to its more common winter state until the final warming (March), after which the stratosphere transforms into its summer state, featuring a westward circumpolar vortex.

Nearly 36 years after its last eruption, Mount Tolbachik began erupting again on 27 November 2012, leading to the largest basaltic eruption in Kamchatka during historic times. The volcanic activity remained high for 9 months and finally weakened at the end of August 2013 [Albert *et al.*, 2015]. Infrasound detections at IS44, at 347 km distance from Mount Tolbachik, provide a near-continuous record of the eruption sequence (Figures 4a and 5a). The relative position of Mount Tolbachik to IS44 as well as the stratospheric dynamics is paramount in understanding the observations. While more volcanoes are present in the area, we assume that infrasound detections for the parameters given in Table 1 correspond to Mount Tolbachik. This seems justified based on activity reports [Smithsonian Institution, 2013]. Moreover, we assume that the source has a constant spectral content.

During the winter period, not including the warming period, infrasound is detected with a relatively large back azimuth offset of $+5^\circ$, when compared to the summer observations (Figure 4a). Taking into account the direction of the winter circumpolar vortex, this suggests that these signals have likely returned from the lower thermosphere instead of the stratopause. After the transition to the summer stratosphere, the back azimuth offset is small and of opposite sign, due to the presence of a westward circumpolar vortex, that creates a stratospheric waveguide. Trace velocities show the expected seasonal signature (Figure 5a) on the basis of

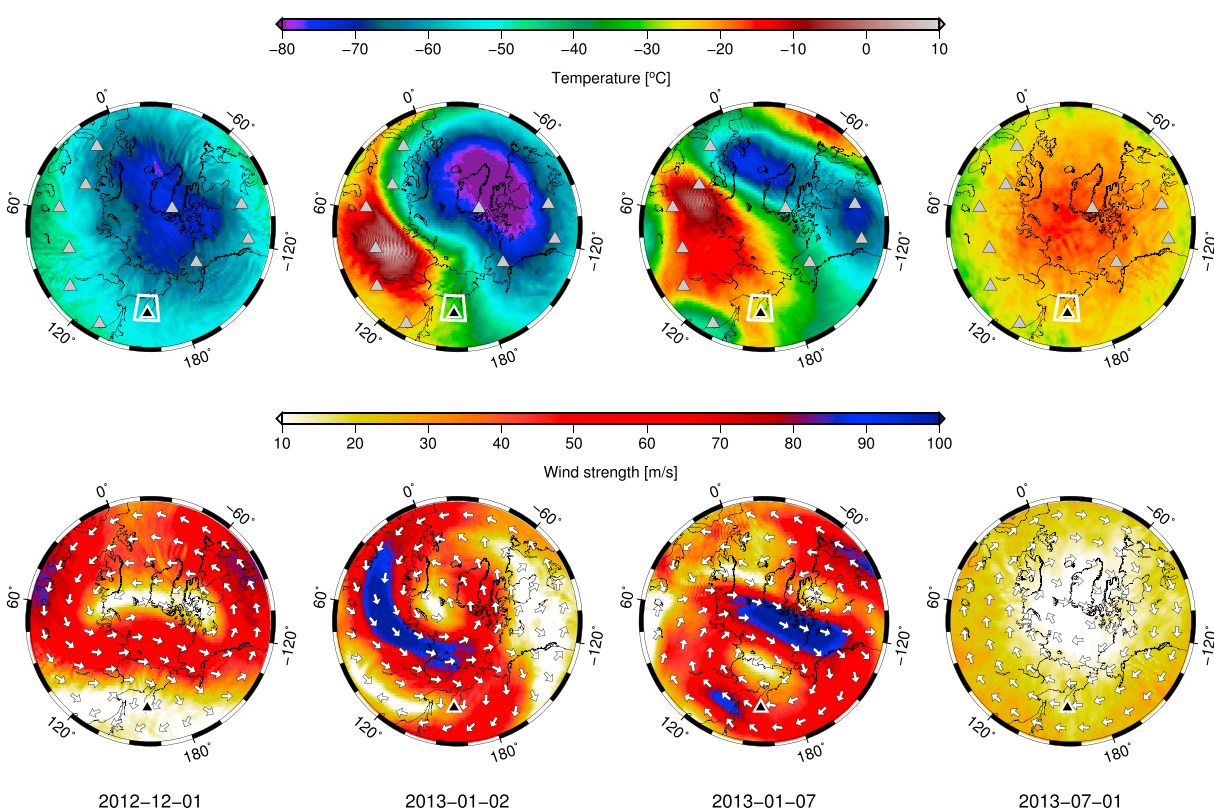


Figure 3. (top row) Temperature and (bottom row) horizontal wind specifications from ECMWF analysis at 5.0 hPa (around 36 km altitude) (first column) before, (second and third columns) during, and (fourth column) after the SSW, which directly influence the detectability of Mount Tolbachik on IS44 (white rectangle).

higher boundary layer temperatures in summer than in winter, with lower velocities in winter and higher in summer. During the SSW, a strong westward vortex is present above the region (Figure 3). As a result, three particularities can be noted. First, the back azimuth deviation rapidly reverses and reaches a much higher value than during the summer. This is in accord with the much stronger westward vortex, i.e., the cross wind causing the back azimuth deviation. Second, the trace velocities are higher than usual and even reach values of 400 m s^{-1} , likely due to the increased temperature and along-track wind. Third, the dominant frequency is significantly higher during the warming period, when compared to the summer. This may be explained by the lower return height during the warming period (30 km as opposed to 45 km; see Figure 6), important for propagation efficiency, resulting in reduced geometrical spreading in combination with reduced absorption of higher frequencies [Lonzaga *et al.*, 2015].

5. Evaluating ECMWF Forecasts

Figure 2 shows an example of stratospheric infrasound propagation, using 3-D ray theory, for three different ECMWF forecasts for 6 January 2013. Typically, IS44 is reached after one bounce. Figure 2a shows the effective sound speed (combining the effect of wind and temperature on infrasound propagation) profiles for the different forecast steps. The largest variability between the different forecasts is found in the upper stratosphere, except for the 10 day forecast, which is different throughout the troposphere and lower stratosphere as well. The sensitivity of infrasound propagation to the variations in forecast steps is essential in this evaluation work.

ECMWF forecasts are evaluated by forward modeling the propagation of infrasound from Mount Tolbachik toward IS44 every 12 h for the entire observation period by 3-D ray theory using the various forecast steps. These wavefront simulations are compared to the array observations in order to validate the atmospheric specifications of each forecast step. Significant inconsistencies or lack of simulated returns indicate a possible difference between the true state of the atmosphere and the consulted forecast in the vicinity of the return height.

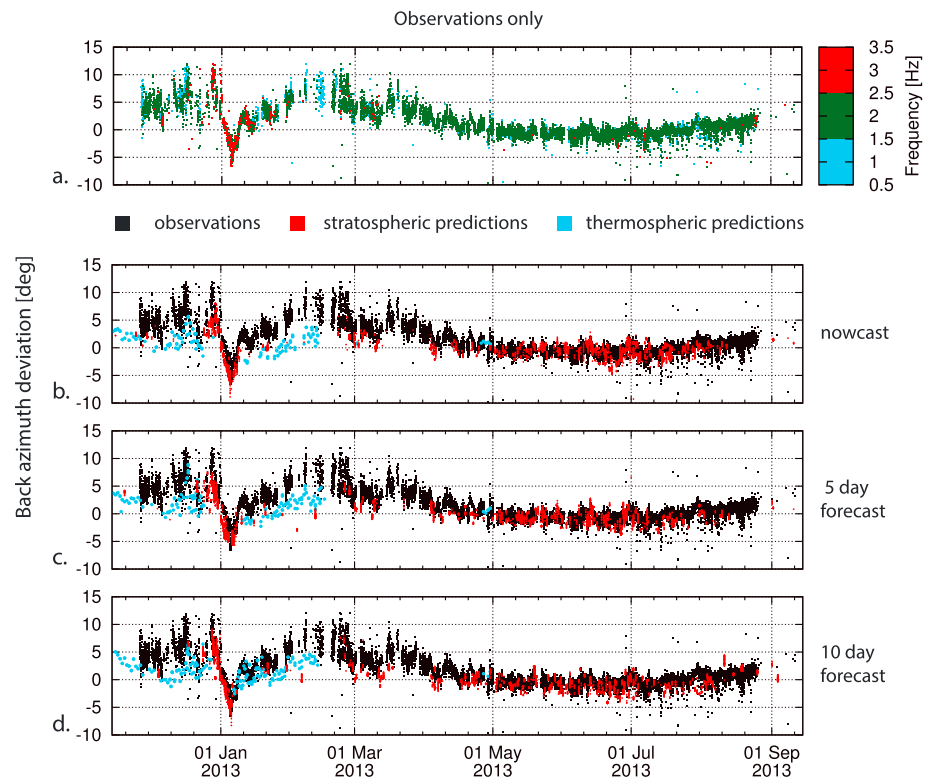


Figure 4. (a) Back azimuth deviation values from Mount Tolbachik infrasound detections, for which trace velocity values are shown in Figure 5a. (b–d) Comparisons between observations (black dots) and 3-D ray tracing results (red dots) as a function of time, using three different ECMWF HRES forecasts: (Figure 4b) nowcast, (Figure 4c) 5 day forecast, and (Figure 4d) 10 day forecast. The blue dots correspond to simulated arrivals that have propagated through the mesosphere and lower thermosphere, for which the MSIS and HWM climatologies have been used.

As mesospheric and thermospheric specifications are missing using the ECMWF IFS, comparison of predictions and observations can be misleading. To explain mesospheric and thermospheric returns, all forecasts are extended with semi-empirical wind and temperature profiles (see section 3.3). In general, observations from mesospheric and thermospheric return heights correspond to observations within the lower frequency range of 0.5–1.5 Hz (see Figures 4 and 5). For these arrivals, there appears to be a near-constant offset of $\pm 2.5^\circ$ (Figure 4), similar to earlier findings by *Le Pichon et al.* [2005]. In their study, the bias between the measurements and the results of simulation is explained by undervalued wind speeds by HWM in the upper atmosphere. Trace velocity values are generally overestimated by 10 to 20 m s^{-1} (Figure 5).

Comparisons of the observed and simulated wavefront characteristics for the entire period of observation, using different forecast steps, are shown in Figures 4 and 5, for back azimuth and trace velocity, respectively. Figures 7 and 8 zoom-in on the period of the SSW. For the sake of brevity, the discussion here is mainly focused on back azimuth deviations although most conclusions hold for the trace velocity observations as well.

The estimated difference between the observed and predicted back azimuth, an indication of the forecast uncertainty, is shown in Figure 9. For each forecast the difference is calculated between the observations (black dots) and predictions (red dots) in Figures 4b–4d. All observations are averaged using 12 h time bins and contain at least six detections (on average, every bin contains 50 detections). In general, uncertainty values of observed back azimuth (horizontal dashed black line in Figure 9) and trace velocity are dependent on the detection slowness, the planarity of the waveform, and the signal-to-noise level [*Szuberla and Olson*, 2004]. For IS44 95% uncertainty values up to 2° and 10 m s^{-1} are possible. In this paper we estimate typical uncertainty values for IS44 1° and 5 m s^{-1} .

5.1. Entire Observation Period

For the entire observation time span the nowcast performs best out of all forecast steps (see Figures 4, 5, and 9a), indicated by a higher continuity of the simulated characteristics and smaller back azimuth differences.

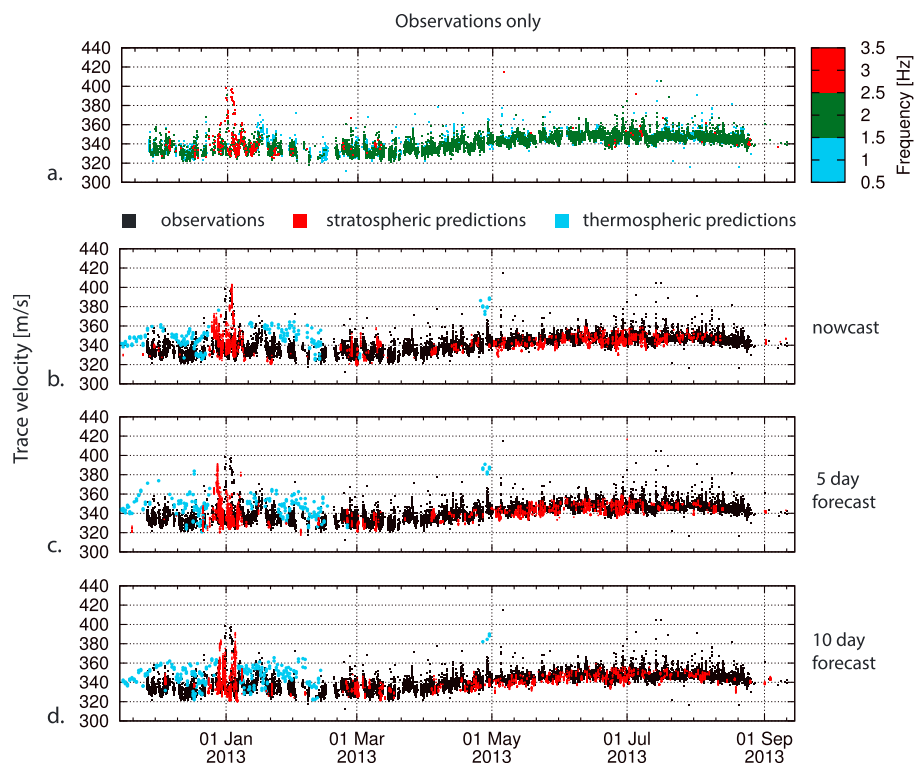


Figure 5. (a) Trace velocity values from Mount Tolbachik infrasound detections. (b–d) Comparisons between observations (black dots) and 3-D ray tracing results (red dots) as a function of time, using three different ECMWF HRES forecasts: (Figure 5b) nowcast, (Figure 5c) 5 day forecast, and (Figure 5d) 10 day forecast. The blue dots correspond to simulated arrivals that have propagated through the mesosphere and lower thermosphere, for which the MSIS and HWM climatologies have been used.

The estimated average back azimuth difference shows a clear seasonal variation with a minimum in summer and differences frequently below the 1° estimated observational uncertainty.

Summer observations, related to the stable summer stratospheric waveguide, are, in general, well simulated by all forecasts up to approximately 10 July 2013. After 10 July 2013, only the nowcast is able to provide continuous predictions (see Figure 9a). Smaller deviations are occasionally obtained using the 5 or 10 day forecasts, though these forecasts do not adequately predict continuous values after 10 July 2013. Despite that the 10 day forecast yields the worst performance, based on the density and continuity of the simulations, it still does provide some sparse predictions until the end of August.

In winter, the stratospheric waveguide is rather unstable, resulting in an increased back azimuth difference almost consistently above the 1° estimated observational uncertainty for all forecasts (see Figure 9a).

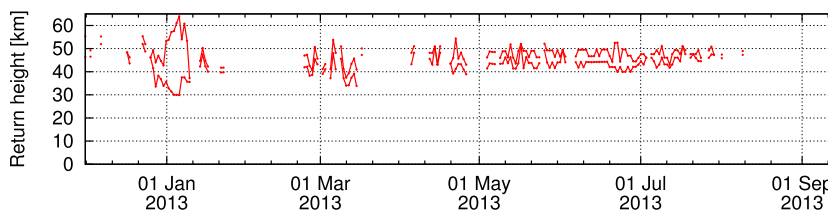


Figure 6. Return height range computed from vertical wind and temperature profiles over IS44 (53°N, 158°E), for propagation from Mount Tolbachik to IS44. During the SSW period, the return heights are lower when compared to the summer (30 km versus 45 km). Lower return height correlates with the higher frequencies observed during the SSW period.

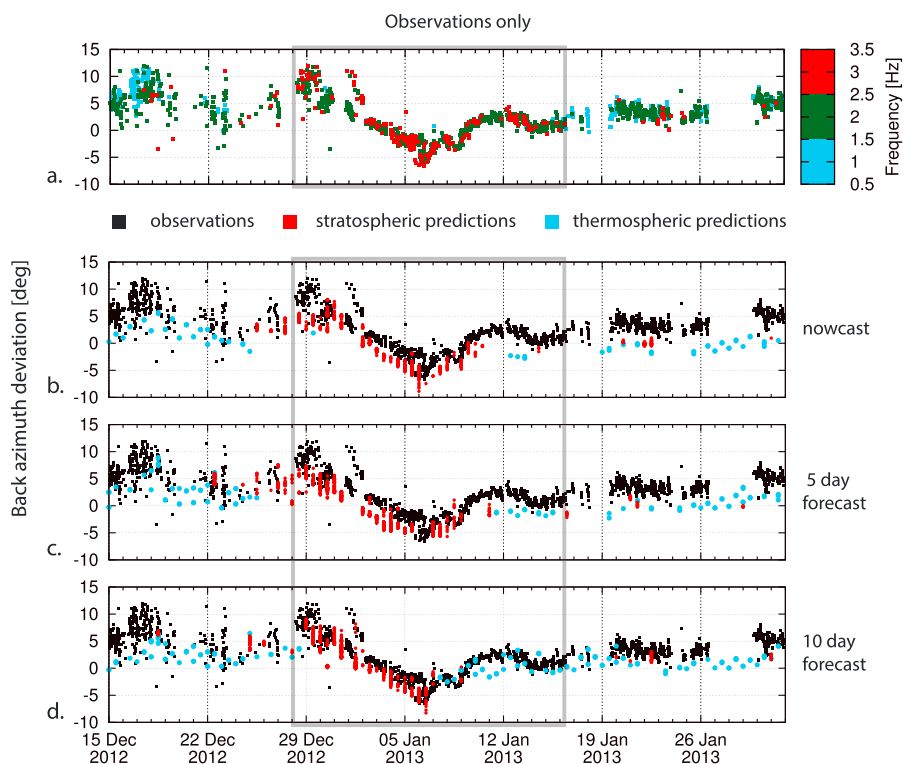


Figure 7. Zooms-in in Figure 4, focusing on the SSW period. The gray rectangle points to the continuous high-frequency infrasound observations interpreted as low stratospheric altitude returns (<40 km return altitude). These low stratospheric returns with sudden reversal in back azimuth are interpreted to be due to the SSW.

5.2. 2013 SSW

Zooming-in on the period of the SSW, see Figures 7 and 8, midwinter stratospheric predictions of back azimuth and trace velocity can only occur due to the dramatic changes in the stratospheric wind and temperature of a SSW. For these unusual winter stratospheric predictions (and during equinox periods), the prediction performance is significantly smaller and clearly different for all three forecast steps when compared to the summer predictions (Figure 9a). The local infrasonic signature of the 2013 SSW observed at IS44 is highlighted in Figures 7 and 8 by the gray rectangle and in Figure 9a by the green rectangle. The rectangle points to the continuous high-frequency infrasound observations interpreted as low stratospheric altitude returns (<40 km return altitude). In addition, these low stratospheric returns are characterized by a sudden reversal in the back azimuth deviation and an increase in trace velocity. Therefore, these low stratospheric returns are interpreted to be due to the SSW indicating the assumed warming onset (28 December 2012) and recovery (16 January 2013).

All forecasts are able to reproduce the general SSW characteristics, including the sudden reversal of the back azimuth deviation (Figures 4 and 7) as well as the sudden increase in trace velocity (Figures 5 and 8). Nevertheless, the performance skill during the SSW is much more variable when compared to the summer predictions.

1. The warming onset (28 December 2012) is well predicted by all three forecasts, both the nowcast and 5 day forecast predict the same warming onset followed 12 h later by the 10 day forecast. Though, the 10 day appears to be more accurate in predicting the larger back azimuth deviations and corresponding trace velocities during the first days of the warming. The resemblance in timing of the predicted and observed stratospheric returns using the 10 day forecast is better as well.
2. During the vortex displacement phase of the major warming (before 7 January 2013), the 10 day forecast most accurately predicts the varying back azimuth deviation, including a sudden wind direction change around 2 January 2013 with corresponding increase in trace velocity (Figure 8). Note that the difference in

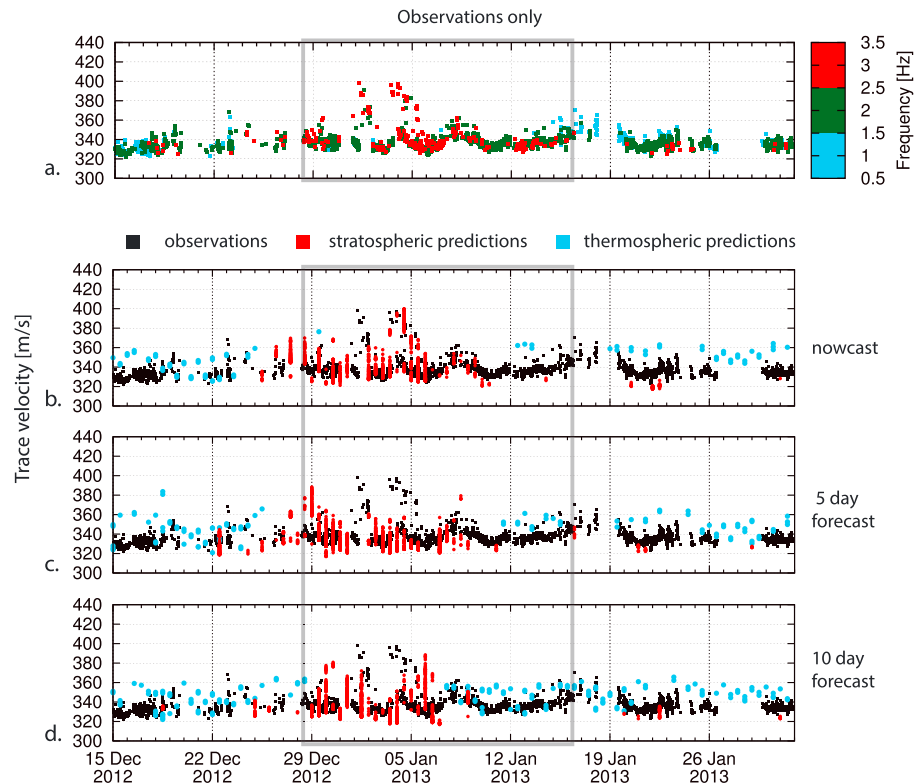


Figure 8. Zooms-in in Figure 5, focusing on the SSW period.

back azimuth prediction of both the nowcast and 10 day forecast is below the array uncertainty. Yet the large difference of the 5 day forecast when compared to the nowcast and 10 day forecast is remarkable.

3. When the vortex splits (around 7 January 2013) the 10 day forecast does no longer predict stratospheric returns, while the 5 day forecast and nowcast continue, respectively, 2 and 4 days with a quasi similar back azimuth difference.

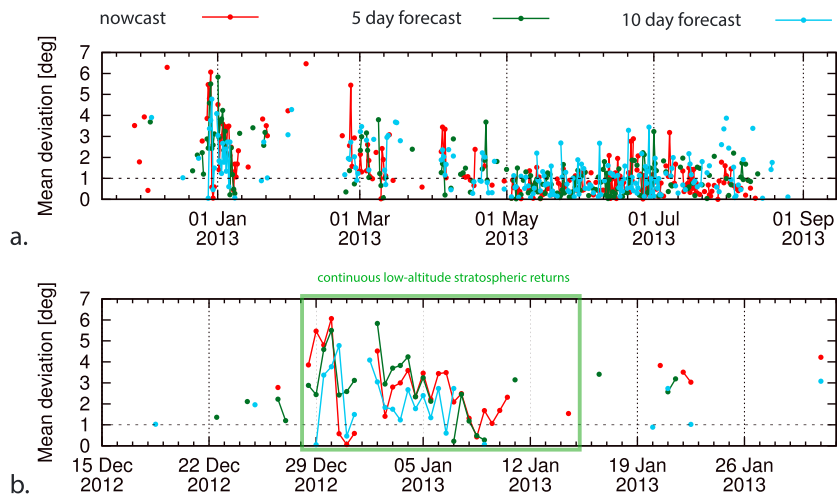


Figure 9. (a) Estimated difference between the observed and predicted back azimuth of all returns over the full time span of observation. Observations are averaged for 12 h time bins and contain at least six detections. The different colors correspond to the different ECMWF forecasts that are used in the simulations. The lines connecting the dots indicate the continuity of the predictions. The horizontal dashed black line is indicative of the uncertainty of the infrasound array. (b) Similar as Figure 9a, but focusing on the midwinter with the SSW period (green rectangle).

4. All forecasts have difficulties to predict the stratospheric observations up to the expected warming recovery (16 January 2013). Predictions for all forecast steps indicate a too-early recovery. The 10 day forecast predicts a difference of about 9 days with respect to the moment that no stratospheric arrivals are expected anymore (8 January 2016). The recovery is best captured by the nowcast model, continuously predicting up to 11 January 2013.

This relative performance is illustrated in Figure 9b, presenting a minimal mean difference between the observed and modeled back azimuth. All forecasts indicate a reduction in back azimuth difference when the vortex migration evolves. Minimal back azimuth differences are obtained using the 10 day forecast, while the nowcast yields the highest continuity of the predictions. Least performance is obtained by the 5 day forecast.

6. Discussion and Conclusions

For the discussion of our results it is important to establish that the nowcast is most constrained by the data assimilation whereas the 10 day forecast tends to be quasi free running, with the 5 day forecast positioned somewhere in between. For a typical forecast, more forecast skill is expected for a shorter forecast step, as it is closer to the data assimilation. This is observed during summer (Figure 9), where the nowcast performs best. Surprisingly, in winter the 10 day forecast appears to be most accurate in predicting the first phase of the warming. For validation, comparison of the nowcast with the subsequent analysis, often applied in NWP, reveals only a small improvement in absolute deviation compared to the nowcast (see Figure S1 in the supporting information). Our interpretation is that the 10 day forecast is able to obtain sufficient information from the small a priori warming signatures with enough time to propagate through the atmosphere, to predict the warming including the sudden recovery around 2 January 2013. Once data have to be assimilated during the warming, the 10 day forecast loses a lot of forecast skill. At this stage, data gets most likely rejected or modified by the data assimilation system leading to inaccurate initialization as addressed by *Diamantakis* [2014]. The nowcast is affected similarly but recovers approximately instantly with the data assimilation system such that it predicts best the SSW duration and recovery.

An ECMWF IFS cycle update has been implemented to address spurious data assimilation issues that occur during SSW events [*Diamantakis*, 2014]. For future research, it would be useful to evaluate the effects of this cycle update (Cy41r1, May 2015), including the consideration of the ensemble forecasts [*Smets et al.*, 2015], using our technique. Moreover, it would be of interest to study the uncertainties due to unresolved small-scale structure, involving 3-D full-wave modeling. Detailed analyses between the various forecasts are needed, for example, by considering differences in polar cap-averaged stratospheric zonal wind and temperature.

For the first time, weather forecasts for different forecast steps are evaluated using infrasound. The high spatiotemporal resolution of infrasound is explained by the relative small wavelength of infrasound (<500 m) compared with the characteristic length scales of atmospheric features (>500 m). The high temporal resolution is due to the use of a near-continuous infrasound source (typical resolution of minutes; compared with 6-hourly atmospheric specifications). The proposed method in this study for the evaluation of middle atmospheric weather forecasts using near-continuous infrasound detections can directly be applied to similar setups, making use of other IMS or even national infrasound arrays. The method presented here relies on an active source like the volcano used. However, source-independent techniques are being developed based on interferometry of the ambient noise field [*Fricke et al.*, 2013, 2014].

This study demonstrates that infrasound can provide useful additional information in regions where data coverage is sparse, such as in the upper stratosphere. The frequency content of the observed infrasound suggests a 6 day longer duration of the 2013 SSW than predicted by the ECMWF nowcast.

Validation of atmospheric analysis and forecast products, in particular in regions above 30 km altitude, is important for numerical weather prediction applications, as the interaction between the stratosphere and the troposphere cannot be neglected. Due to the delayed impact of a warming on the weather at the ground, evaluating the forecast in the middle atmospheric can act as an early indicator of a possible upcoming loss of forecast skill in the troposphere. As atmospheric specifications in the lower and middle atmosphere are routinely used in a wide variety of atmospheric sciences and applications, the validation is relevant to a broad community and a wide variety of applications, such as the verification of the Comprehensive Nuclear-Test-Ban Treaty, in which infrasound is used as a verification technique.

Acknowledgments

We thank Adrian Simmons (ECMWF) for the discussions and review of the initial manuscript. This work was performed during the course of the ARISE design study (<http://arise-project.eu>), from the European Union within FP7, grant 284387, and the ARISE2 project within H2020, project 653980. L.E.s contribution is partly funded through a VIDJ project from the Dutch Science Foundation (NWO), project 864.14.005. The authors thank the CTBTO and station operators for the high quality of IMS data and products. The data for this paper from CTBTO and ECMWF are available to member states but can be requested for academic purposes. Infrasound data can be requested at the CTBTO International Data Centre (IDC) in Vienna, via the virtual Data Exploration Centre (vDEC). Atmospheric data can be requested at the ECMWF via the Meteorological Archival and Retrieval System (MARS). Figures 1–3 in this article are made with the Generic Mapping Tools [Wessel and Smith, 1991].

References

- Albert, S., D. Fee, P. Firstov, E. Makhmudov, and P. Izbekov (2015), Infrasound from the 2012–2013 Plosky Tolbachik, Kamchatka fissure eruption, *J. Volcanol. Geotherm. Res.*, *307*, 68–78.
- Assink, J. D., R. Waxler, and D. P. Drob (2012), On the sensitivity of infrasonic traveltimes in the equatorial region to the atmospheric tides, *J. Geophys. Res.*, *117*, D01110, doi:10.1029/2011JD016107.
- Assink, J. D., R. Waxler, W. G. Frazier, and J. Lonzaga (2013), The estimation of upper atmospheric wind model updates from infrasound data, *J. Geophys. Res. Atmos.*, *118*, 10,707–10,724, doi:10.1002/jgrd.50833.
- Assink, J. D., A. L. Pichon, E. Blanc, M. Kallel, and L. Khemiri (2014a), Evaluation of wind and temperature profiles from ECMWF analysis on two hemispheres using volcanic infrasound, *J. Geophys. Res. Atmos.*, *119*, 8659–8683, doi:10.1002/2014JD021632.
- Assink, J. D., R. Waxler, P. Smets, and L. G. Evers (2014b), Bi-directional infrasonic ducts associated with sudden stratospheric warming events, *J. Geophys. Res. Atmos.*, *119*, 1140–1153, doi:10.1002/2013JD021062.
- Baldwin, M. P., and T. J. Dunkerton (2001), Stratospheric harbingers of anomalous weather regimes, *Science*, *294*, 581–584.
- Brachet, N., D. Brown, R. L. Bras, Y. Cansi, P. Mialle, and J. Coyne (2010), Monitoring the Earth's atmosphere with the global IMS infrasound network, in *Infrasound Monitoring for Atmospheric Studies*, edited by A. Le Pichon, E. Blanc, and A. Hauchecorne, chap. 3, pp. 77–118, Springer, New York.
- Brekhovskikh, L. M., and O. A. Godin (1999), *Acoustics of Layered Media II: Point Sources and Bounded Beams*, Springer Series on Wave Phenomena, vol. 10, chap. 4–5, p. 524, Springer, Berlin.
- Charlton, A. J., and L. M. Polvani (2007), A new look at stratospheric sudden warmings. Part I: Climatology and modeling benchmarks, *J. Clim.*, *20*, 449–469.
- Charlton, A. J., A. O'Neill, W. A. Lahoz, and A. C. Massacand (2004), Sensitivity of tropospheric forecasts to stratospheric initial conditions, *Q. J. R. Meteorol. Soc.*, *130*, 1771–1792.
- Charlton-Perez, A. J., et al. (2013), On the lack of stratospheric dynamical variability in low-top versions of the CMIP5 models, *J. Geophys. Res. Atmos.*, *118*, 2494–2505, doi:10.1002/jgrd.50125.
- Chunchuzov, I., S. Kulichkov, V. Perepelkin, O. Popov, P. Firstov, J. D. Assink, and E. Marchetti (2015), Study of the wind velocity layered structure in the stratosphere, mesosphere and lower thermosphere by using infrasound probing of the atmosphere, *J. Geophys. Res. Atmos.*, *120*, 8828–8840, doi:10.1002/2015JD023276.
- Coy, L., S. D. Eckermann, K. W. Hoppel, and F. Sassi (2011), Mesospheric precursors to the major stratospheric sudden warming of 2009: Validation and dynamical attribution using a ground-to-edge-of-space data assimilation system, *J. Adv. Model. Earth Syst.*, *3*, M10002.
- Dahlman, O., S. Mykkeltveit, and H. Haak (2009), *Nuclear Test Ban: Connecting Political Views to Reality*, Springer, pp. 113–142, Netherlands.
- Diamantakis, M. (2014), Improving ECMWF forecasts of sudden stratospheric warmings, *ECMWF Newsletter*, *141*, 30–36.
- Donn, W. L., and D. H. Rind (1971), Natural infrasound as an atmospheric probe, *Geophys. J. R. Astron. Soc.*, *26*, 111–133.
- Donn, W. L., and D. H. Rind (1972), Microbaroms and the temperature and wind of the upper atmosphere, *J. Atmos. Sci.*, *29*, 156–172.
- Drob, D. P., et al. (2008), An empirical model of the Earth's horizontal wind fields: HWM07, *J. Geophys. Res.*, *113*, A12304, doi:10.1029/2008JA013668.
- European Centre for Medium-Range Weather Forecasts (2016), Changes in ECMWF model. [Available at <http://www.ecmwf.int/en/forecasts/documentation-and-support/changes-ecmwf-model>.]
- Evers, L. G., and P. Siegmund (2009), Infrasonic signature of the 2009 major Sudden Stratospheric Warming, *Geophys. Res. Lett.*, *36*, L23808, doi:10.1029/2009GL041323.
- Evers, L. G., A. van Geyt, P. Smets, and J. Fricke (2012), Anomalous infrasound propagation in a hot stratosphere and the existence of extremely small shadow zones, *J. Geophys. Res.*, *117*, D06120, doi:10.1029/2011JD017014.
- Fee, D., A. Steffke, and M. Garces (2010), Characterization of the 2008 Kasatochi and Okmok eruptions using remote infrasound arrays, *J. Geophys. Res.*, *115*, D00L10, doi:10.1029/2009JD013621.
- Fricke, J. T., N. El Allouche, D. G. Simons, E. N. Ruigrok, K. Wapenaar, and L. G. Evers (2013), Infrasonic interferometry of stratospherically refracted microbaroms—A numerical study, *J. Acoust. Soc. Am.*, *134*, 2660–2668.
- Fricke, J. T., L. G. Evers, P. S. M. Smets, K. Wapenaar, and D. G. Simons (2014), Infrasonic interferometry applied to microbaroms observed at the large aperture infrasound array in the Netherlands, *J. Geophys. Res. Atmos.*, *119*, 9654–9665, doi:10.1002/2014JD021663.
- Gerber, E. P., C. Orbe, and L. M. Polvani (2009), Stratospheric influence on the tropospheric circulation revealed by idealized ensemble forecasts, *Geophys. Res. Lett.*, *36*, L24801, doi:10.1029/2009GL040913.
- Godin, O. A. (2002), An effective quiescent medium for sound propagating through an inhomogeneous, moving fluid, *J. Acoust. Soc. Am.*, *112*, 1269–1275.
- Lalande, J.-M., O. Sèbe, M. Landès, P. Blanc-Benon, R. Matoza, A. L. Pichon, and E. Blanc (2012), Infrasound data inversion for atmospheric sounding, *Geophys. J. Int.*, *190*, 687–701.
- Le Pichon, A., E. Blanc, D. P. Drob, S. Lambotte, J. X. Dessa, M. Lardy, P. Bani, and S. Vergnolle (2005), Infrasound monitoring of volcanoes to probe high-altitude winds, *J. Geophys. Res.*, *110*, D13106, doi:10.1029/2004JD005587.
- Le Pichon, A., et al. (2015), Comparison of co-located independent ground-based middle-atmospheric wind and temperature measurements with Numerical Weather Prediction models, *J. Geophys. Res. Atmos.*, *120*, 8318–8331, doi:10.1002/2015JD023273.
- Lonzaga, J. B., R. Waxler, J. D. Assink, and C. Talmadge (2015), Modelling waveforms of infrasound arrivals from impulsive sources using weakly non-linear ray theory, *Geophys. J. Int.*, *200*, 1347–1361.
- Marchetti, E., M. Rippepe, D. Delle Donne, R. Genco, A. Finizola, and E. Garaebiti (2013), Blast waves from violent explosive activity at Yasur Volcano, Vanuatu, *Geophys. Res. Lett.*, *40*, 5838–5843, doi:10.1002/2013GL057900.
- Matoza, R., et al. (2011), 2 of the Eyjafjallajökull eruption, Iceland, April–May 2010, *Geophys. Res. Lett.*, *38*, L06308.
- Matsuno, T. (1971), A dynamical model of stratospheric warmings, *J. Atmos. Sci.*, *28*, 1479–1494.
- Picone, J. M., A. Hedin, D. Drob, and A. Aikin (2002), NRL MSISE-00 empirical model of the atmosphere: Statistical comparisons and scientific issues, *J. Geophys. Res.*, *107*, 1468, doi:10.1029/2002JA009430.
- Pierce, A. D. (1981), *Acoustics—An Introduction to Its Physical Principles and Applications*, McGraw-Hill Series in Mechanical Engineering, McGraw-Hill, New York.
- Ponceau, D., and L. Bosca (2010), Low-noise broadband microbarometers, in *Infrasound Monitoring for Atmospheric Studies*, edited by A. Le Pichon, E. Blanc, and A. Hauchecorne, pp. 119–140, Springer, New York, chap. 4.
- Ramaswamy, V., et al. (2001), Stratospheric temperature trends: Observations and model simulations, *Rev. Geophys.*, *39*, 71–122.
- Randel, W., et al. (2004), The SPARC intercomparison of middle-atmosphere climatologies, *J. Clim.*, *17*, 986–1003.
- Rind, D. H. (1978), Investigation of the lower thermosphere results of ten years of continuous observations with natural infrasound, *J. Atmos. Sol. Terr. Phys.*, *40*, 1199–1209.

- Rind, D. H., and W. L. Donn (1975), Further use of natural infrasound as a continuous monitor of the upper atmosphere, *J. Atmos. Sci.*, *32*, 1694–1699.
- Roff, G., D. W. J. Thompson, and H. Hendon (2011), Does increasing model stratospheric resolution improve extended-range forecast skill?, *Geophys. Res. Lett.*, *38*, L05809, doi:10.1029/2010GL046515.
- Shaw, T. A., and T. G. Shepherd (2008), Raising the roof, *Nat. Geosci.*, *1*, 12–13.
- Sigmond, M., J. F. Scinocca, V. V. Kharin, and T. G. Shepherd (2013), Enhanced seasonal forecast skill following Stratospheric Sudden Warmings, *Nat. Geosci.*, *6*, 98–102.
- Smets, P. S. M., and L. G. Evers (2014), The life cycle of a Sudden Stratospheric Warming from infrasonic ambient noise observations, *J. Geophys. Res. Atmos.*, *119*, 12,084–12,099, doi:10.1002/2014JD021905.
- Smets, P. S. M., L. G. Evers, S. P. Näsholm, and S. J. Gibbons (2015), Probabilistic infrasound propagation using realistic atmospheric perturbations, *Geophys. Res. Lett.*, *42*, 6510–6517, doi:10.1002/2015GL064992.
- Smithsonian Institution (2013), Global Volcanism Program. [Available at <http://www.volcano.si.edu/world>.]
- Sutherland, L. C., and H. E. Bass (2004), Atmospheric absorption in the atmosphere up to 160 km, *J. Acoust. Soc. Am.*, *115*, 1012–1030.
- Szuberla, C., and J. Olson (2004), Uncertainties associated with parameter estimation in atmospheric infrasound arrays, *J. Acoust. Soc. Am.*, *115*, 253–258.
- Wessel, P., and W. Smith (1991), Free software helps map and display data, *Eos Trans. AGU*, *72*, 441–446.